

# Deformation and fracture behavior of new strain-transformable titanium alloys: a multi-scale investigation.

Chloé VARENNE<sup>a,b</sup>, Frédéric PRIMA<sup>b</sup>, Cédrik BROZEK<sup>b</sup>, Julie BOURGON<sup>c</sup>, Jacques BESSON<sup>a</sup>,

Anne-Françoise GOURGUES-LORENZON<sup>a</sup>

<sup>a</sup> MINES ParisTech, PSL Research University, Centre des Matériaux, UMR CNRS 7633, BP 87, 91003 Evry cedex, France

<sup>b</sup> PSL Research University, Chimie ParisTech-CNRS, Institut de Recherche de Chimie Paris, 75005 PARIS, France

<sup>c</sup> UPE Université Paris Est, ICMPE (UMR 7182) CNRS-UPEC, 94320, Thiais, France

## **Abstract**

Titanium alloys possessing Twinning and Transformation Induced Plasticity effects show promising mechanical properties, particularly high ductility, hardenability, impact and fracture toughness. This work focuses on a strain-transformable, coarse-grained  $\beta$ -Ti-Cr-Sn alloy displaying TWIP effect. To account for the enhanced properties of this alloy, compared to more conventional  $\beta$ -Ti alloys, fracture and deformation features were correlated at different scales. Examinations evidenced a major role of twinning and, more generally, of plasticity-induced phenomena in the ductile fracture process. The resistance of this alloy to plastic deformation (work-hardening), and to crack initiation and propagation is interpreted in view of the progressive, multiscale twinning mechanisms that occur up to the very final stages of fracture.

## **1. Introduction**

Conventional  $\beta$ -titanium alloys show moderate ductility (typically, around 15 %) and work-hardening (typically, around 80 MPa), which limit their use in some structural applications despite their moderate density. The concept of twinning induced plasticity (TWIP) austenitic steels with improved properties, through the “dynamic Hall-Petch” effect (progressive microstructural refinement), was transposed to bcc  $\beta$ -titanium alloys. This led to a new generation of strain-transformable  $\beta$ -Ti alloys, with much higher ductility and work hardenability than those of conventional  $\beta$ -Ti alloys [1]. A semi-empirical approach was used to design these new alloys, linking chemistry to deformation mechanisms. This method was successfully used on binary, ternary and quaternary alloys [2].

The mechanical behavior of these promising alloys still raises numerous questions; in particular, little has been reported about interactions between plasticity mechanisms and fracture mechanisms. The aim of this work is to investigate the singularities of a  $\beta$ -metastable Ti-8.5Cr-1.5Sn TWIP alloy compared to other titanium alloys. A new method to link fracture and plastic deformation features is firstly presented and applied under various mechanical testing conditions; then, a fracture scenario is proposed for this alloy.

## **2. Materials and experiments**

A Ti-8.5Cr-1.5Sn (wt.%) alloy (denoted as TCS) was provided as a hot-rolled plate showing  $\alpha+\beta$  microstructure. It was flash heat treated in molten salt baths at 1023 K (750 °C, 25 °C above the  $\beta$  transus) for 10 min and subsequently water quenched. The resulting full  $\beta$ -metastable microstructure showed an average grain size of 600 $\mu$ m. Such a coarse grain size was used to investigate the complex fracture and deformation mechanisms on a grain-by-grain basis.

Uniaxial tensile tests were performed on flat dogbone-shaped specimens, with a gauge length of 35 mm, on a servo hydraulic MTS facility. Round notched specimens, with a gauge diameter of 6 mm and a notch diameter of 4.80 mm (denoted as NT4), were also tested. All specimens were tested at room temperature along the rolling direction.

Crack advance ( $Da$ ) was evaluated using the unloading compliance method [3] on conventional pre-cracked 12.5-millimeter compact tension (CT) specimens, on a INSTRON 8500 servo hydraulic facility. Specimens were taken both along the rolling (L) and long transverse (T) directions, with the crack propagation direction respectively aligned with T (LT orientation) and L directions (TL orientation).

Charpy ISO-V impact tests were performed on conventional impact specimens [4], on a 450J-capacity Zwick/Roell instrument. The specimens were taken along the rolling direction with the crack propagation direction aligned with the T direction (LT orientation).

After testing, fractographic and microstructural examinations were performed with a high-resolution Keyence optical microscope (OM) and with a field emission gun scanning electron microscope (SEM), equipped with electron backscatter diffraction (EBSD) on longitudinal and transverse sections. These sections were ground, and then polished with a colloidal silica finish. Except for damage and EBSD analyses, they were etched using Kroll's reagent (3 % HF, 6 % HNO<sub>3</sub>, 91 % H<sub>2</sub>O) for 10 s. EBSD scans were performed with a step size of 1 μm, a tilt angle of 70° and a high voltage of 20 kV.

Transmission electron microscopy (TEM) analyses were performed using a 200 kV Tecnai F20 field emission TEM equipped with Precession-Assisted Crystal Orientation Mapping (PACOM) ASTAR system [5]. Thin foils were prepared from a 3 mm diameter cylinder taken across the fracture surface of one V-Charpy specimen, 4 mm from the notch front line and parallel to it. Five thin foils were prepared, by first mechanical polishing down to a thickness around 100μm and then twin-jet thinning with an electrolyte containing perchloric acid, methanol and 2-butoxyéthanol at 243 K (-30 °C) and 27 V.

### 3. Results

#### Macroscopic mechanical behavior

Tensile tests on flat smooth specimens evidenced a high uniform elongation, ranging between 20 and 30 %, as well as high work hardening for the TCS alloy (Fig. 1.a). Among β-Ti alloys, its Young modulus is higher than that of Ti-12 Mo and similar to that of β-Ti-10Fe-2Fe-3Al (β-Ti-10-2-3). The TCS alloy also had an improved homogeneous elongation compared to TA6V and Ti-10-2-3. Yield and ultimate tensile stresses (YS and UTS) as well as hardening and elongation to fracture are summarized in Table 1. The reduction of area to fracture, evidencing the ultimate ductility, is also indicated in this table, when available.

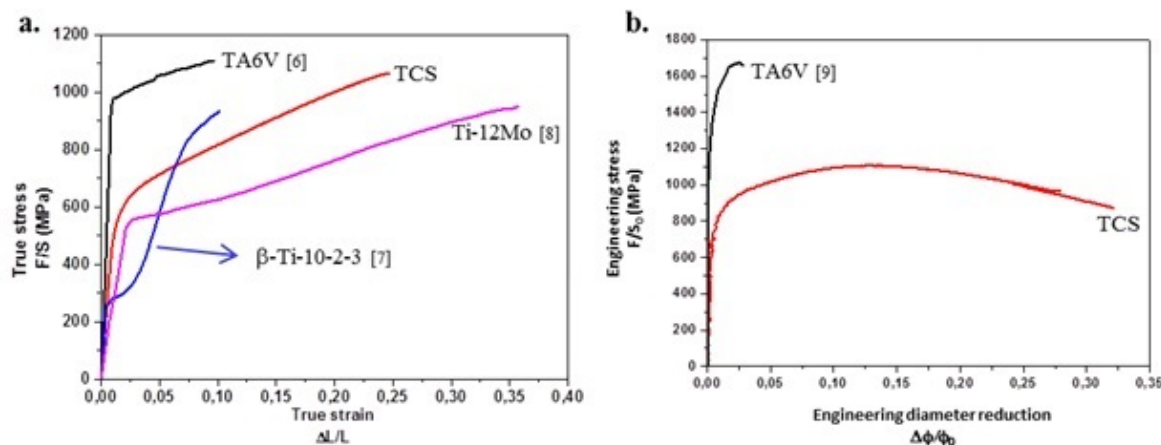


Fig. 1: a. Uniaxial true stress-true strain tensile curves of four Ti alloys [6][7][8];

b. Available net stress vs. diameter reduction curves from notched tensile NT4 specimens [9]

Tensile tests on round notched specimens were performed to assess the resistance to strain localization. The TCS alloy shows a diameter reduction at fracture of 30 % in average, which is really high, compared to the 5-per-cent diameter reduction for TA6V (Fig. 1.b). Moreover, whatever the initial notch radius (2.4 or 4.8 mm here) the diameter reduction remained in the same range for the TCS alloy (25 – 35 %). Finally, even at the end of the test (the specimen was unloaded once the load dropped under 50 % of the maximum load) specimens were not completely broken. Macroscopic observations revealed that the crack propagated from the notch root of the specimens toward the center, which is not usually reported for round notched specimens, especially in the case of ductile fracture.

These unusual crack initiation and propagation modes were further investigated with *J*-*Da* tests, on LT and TL specimens. The *J*-*Da* plots (Fig. 2.a) evidenced a high resistance to crack initiation, as shown of the high value of *J*<sub>0,2</sub> (Table 1). Once initiation was completed, little energy was needed to propagate the crack, which shows that crack propagation is relatively easy, even if macroscopically stable in the TCS alloy. Fracture toughness values were also calculated for the three compared alloys (Table 1), assuming small scale plasticity and plane strain loading conditions (equation 1). It evidences that the TCS alloy shows a high toughness compared to conventional αβ and β-Ti alloys.

$$J = K_{Jc}^2 \left( \frac{1 - \nu^2}{E} \right) \quad (1)$$

The impact toughness of the TCS alloy was evaluated using the Charpy tests, involving high-speed loading (typical local strain rates ~ 100 s<sup>-1</sup>). The values of the impact resistance of the four compared Ti alloys are summarized in Table 1. The unprecedented value of impact toughness of TCS is again higher compared to that of both other alloys.

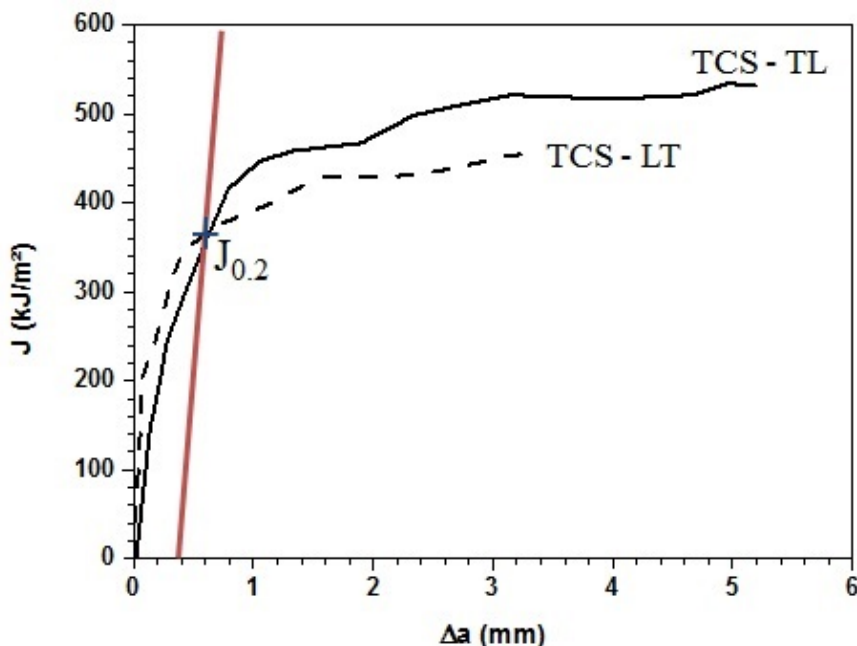


Fig. 2: *J*-*da* curves of two TCS compact tension (CT) specimens;

Table 1: TCS, TA6V, Ti10-2-3 and Ti-12 Mo mechanical properties.

Alloy	TCS	TA6V	b-Ti-10-2-3	b-Ti-12Mo
<b>0.2 % proof stress, YS (MPa)</b>	695	800 - 1000	260	500
<b>Ultimate tensile strength, UTS (MPa)</b>	835	1050 - 1100	880	1000
<b>Young modulus (GPa)</b>	75	100 - 110	60	30
<b>Work hardening ability (UTS-YS, MPa)</b>	140	100 - 110	620	500
<b>Fracture elongation (%)</b>	25	5 - 10	5 - 12	40
<b>Average area reduction to fracture (%)</b>	40	25	-	-
<b>Average <math>J_{0.2}</math> (kJ/m<sup>2</sup>)</b>	310	100	65	same
<b>Average <math>K_{Jc}</math> (MPa.m<sup>0.5</sup>)</b>	160	112	65	range
<b>Average <i>KV</i> (J)</b>	159	60	40	as TCS
<b>Reference</b>	-	[9][12]	[7][11]	[8]

*Physical deformation and fracture mechanisms*

The etched cross-section of the deformed part of Charpy specimen revealed a high density of deformation bands (Fig. 3.a). A region extending over 8mm below the fracture surface was significantly plastically deformed: close to the fracture surface there was a highly deformed zone (region A in Fig. 3.a) where the etched specimen had whitened during etching; below that region, a significantly deformed zone was identified (region B in Fig. 3.a), where deformation bands were also revealed (bright color) by etching but in lower density. No deformation band could be observed further from the fracture surface.

Orientation imaging analyses (Fig. 3.c in highly deformed zone A, Fig. 3.d in significantly deformed zone B) were performed on one Charpy specimen. Zone A was only examined using PACOM because of the high deformation induced by the high density of deformation bands.

The {332}<113> twinning system was evidenced using EBSD in zone B (Fig. 3.d) [13][14]. The thickness of these twins and distance between them are reported in Table 2. The fraction of such twins was quantified by band pass filtering and IQ grey level thresholding, yielding a value of 48%. These investigations are illustrated here on the Charpy specimen only but carried out on all specimens. They all yielded similar results, confirming that deformation mechanisms are multi-scaled and highly localized and similar under quasi-static and under impact loading conditions.

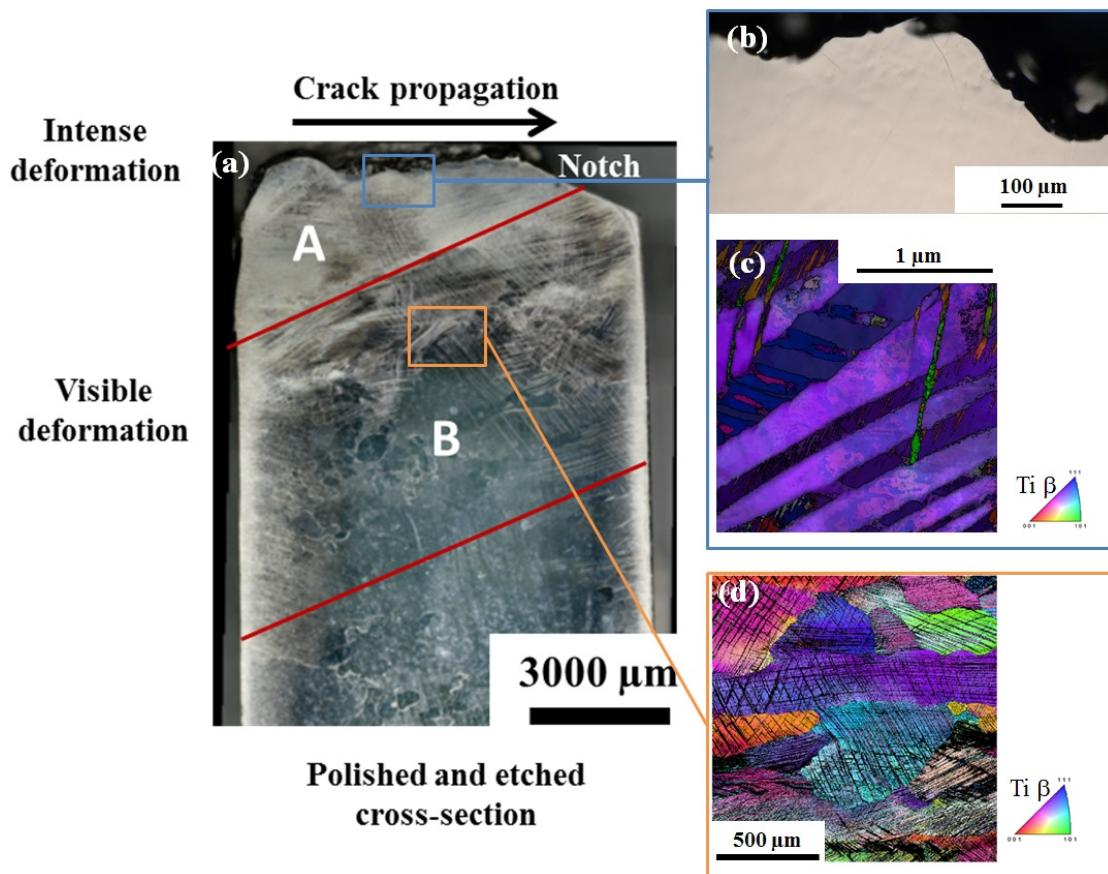


**Fig. 3:** Optical microscopy image of a. the etched mid-thickness cross-section of a Charpy specimen, b. the top of the cross section to evidence no damage; c. PACOM-TEM orientation imaging micrograph of a thin foil taken across the fracture surface the same Charpy specimen; d. EBSD orientation imaging micrograph below the fracture surface; inverse pole figure maps (tensile direction) are superimposed with Image Quality (IQ)

PACOM analysis of zone A (Fig. 3.c) revealed the presence of finer, secondary twins, from both  $\{332\}\langle 113 \rangle$  and  $\{112\}\langle 111 \rangle$  twinning systems usually reported in TWIP-aided titanium alloys [1, 13-16]. The thickness and interspacing of these twins are indicated in Table 2. Distances were measured from PACOM images and confirmed on a larger statistical basis with SEM imaging of the etched cross-section.

The matrix and twin deformation was analyzed in-depth, combining virtual bright field and IPF maps. Dislocation bands and high misorientation (Fig. 3.c) can be spotted within some twins and within the matrix. This evidences the contribution of dislocations to the high local deformation inside these twins, as well as to the high deformation of the matrix.

Fractographic observations were performed on each type of specimens. First, any damage in the fracture process zone was searched from cross-sections of both a round notched and a Charpy specimen. Figure 3.a and b evidence the absence of damage on the Charpy cross-section, even close to the fracture surface. First observations of the fracture surface showed that it was covered with dimples, characteristic of a ductile fracture mechanism. Two dimple populations were visible, as evidenced in Fig. 4.b: small, shallow dimples and large, deeper dimples. Various morphologies were observed on the fracture surface: macro-cavities (Fig. 4.a) composed of dimples (Fig. 4.b) or of smooth features. Dimple walls displayed some plasticity ridges (Fig. 4.e). Between dimpled areas, vein-like areas can also be observed consisting of aligned, unclosed dimples (Fig. 4.c-d). However, dimples do not show any visible feature to explain their nucleation. From dimple characterization and microstructural observations, the TCS alloy, studied here and in [1, 11], is confirmed to be single-phased, showing no second phase particle or inclusion where fracture could initiate from. Thus, attention was paid to the characteristic length scales of the fracture features in order to link them to the characteristic length scales of deformation features. Characteristic sizes of all features are summarized in Table 2.

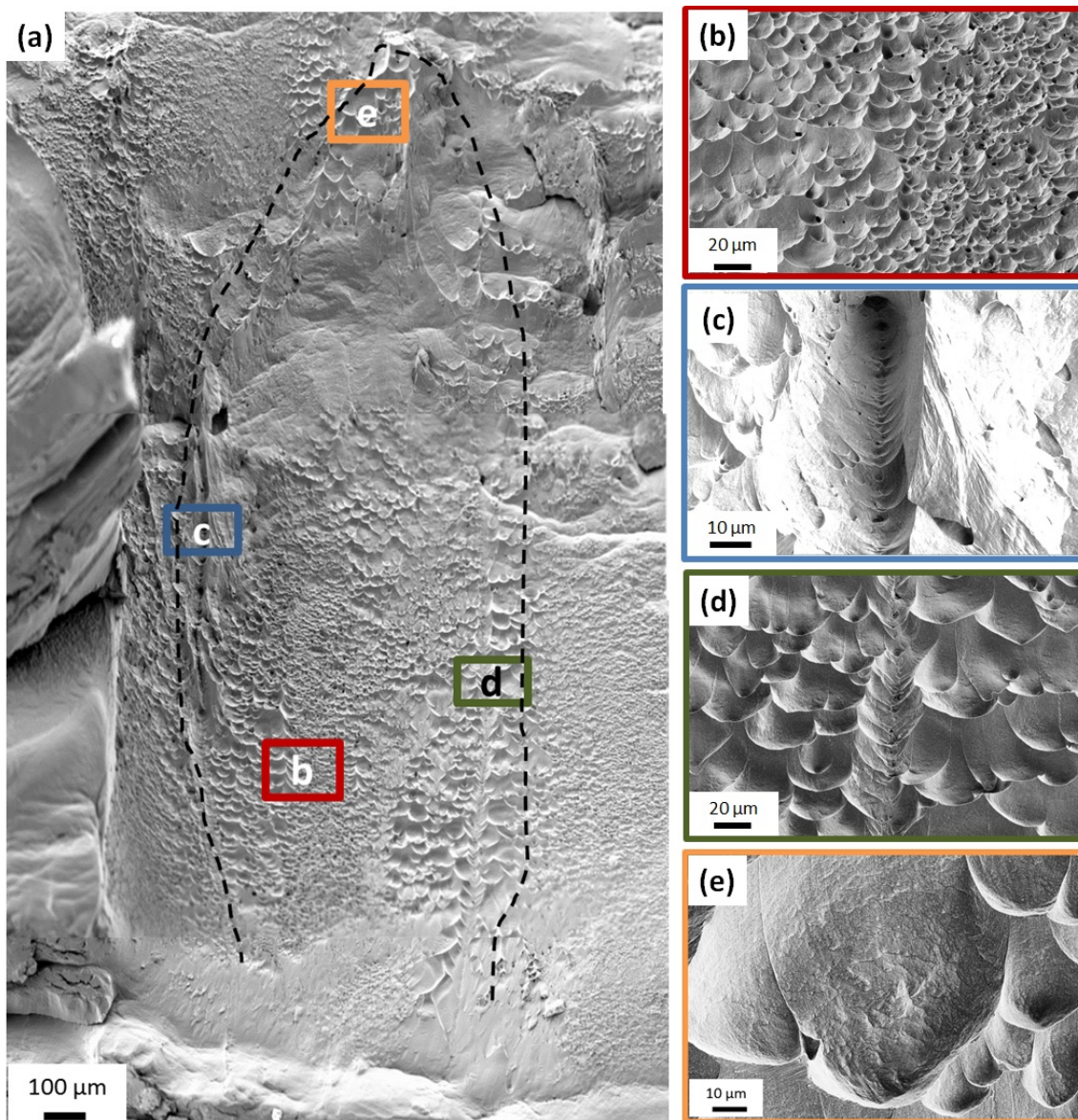


Fig. 4: a-e. SEM images under secondary electron mode of a. macro-cavity (delimited by black dashed line) composed of b. two-sized dimples, c. d. vein-like areas composed of aligned, incompletely closed dimples; e. plasticity ridges inside a dimple

Table 2. Characteristic length scales of the different deformation and fracture features as observed in Charpy specimens

Deformation feature	Size (μm)	Fracture feature	Size (μm)
Average beta grain size	750	Macro-cavities	500 - 800
Primary twins thickness (i.e. indexed by EBSD)	5 - 15	Dimples (equivalent circle diameter)	2 - 35
Distance between primary twins	20 - 80	Vein-like area	1 - 6
Secondary twin thickness (i.e. indexed by PACOM analysis)	0.1 - 0.4	Plasticity ridges	30 - 50
Distance between secondary twins	0.5 - 5		5 - 10

#### 4. Discussion: Ti-Cr-Sn fracture and deformation mechanisms - current state of understanding

Table 2 evidences some parallels between the respective size ranges of fracture and deformation features. This suggests that the plasticity mechanisms could play a central role both in deformation and fracture, including void initiation.

The large deformation ability of twins themselves, despite their fine thickness, was evidenced with the observation of internal twinning of twins (Fig. 4.b), which we call a “self-similar” mechanism hereafter. This mechanism is specific to bcc TWIP-aided Ti

alloys, and has not been reported in fcc TWIP-aided steels. The ductility of TWIP steels stems from high work-hardening that delays strain localization but twins cannot deform easily themselves, so that fracture occurs abruptly right after the onset of necking [17]. On the other hand, TWIP-aided Ti alloys still show a high work hardening as evidenced in Fig. 1.a and additional strain is brought by the deformation of twins, even after the onset of necking and of crack propagation, either with the self-similar mechanism (Fig. 4.b) or by dislocation glide.

Following these analyses, we can propose a first hypothesis for the fracture scenario in this alloy. The macroscopic external stress  $\sigma_{ex}$  triggers twin nucleation and growth, leading to a very fast microstructural refinement. Therefore, even if the initial microstructure is coarse, the crack has to initiate in a refined microstructure. This process is difficult because of the still high deformation ability of the fine microstructure, including fine twins produced by the self-similar twinning mechanism. On the other hand, the crack initiates from a highly twinned zone where the local stress might be much higher than in the rest of the material. Indeed, the needle-like shape of twins and the plastic strain incompatibility at twin/matrix interfaces, particularly close to parent grain boundaries, could induce high local stress triaxiality leading to void nucleation. The crack then propagates in this multi-scale microstructure, always deformable at a lower scale (micro sub-micro and nano scales) until a final point. This makes crack propagation easier than the initiation process. Globally, the parent  $\beta$  grain contribution to fracture remains visible on the fracture surface, as parent grain boundaries are the main loci of crack deviation (Fig. 3.c). This suggests that unstable crack propagation could occur within one parent grain; this agrees with audible events that were heard during the compliance tests.

## **5. Conclusion**

In this work, several peculiarities of the TCS alloy regarding fracture and deformation were evidenced:

- High values of work hardening, fracture toughness and impact toughness, as well as an improved ductility and an unprecedented resistance to strain localization were obtained for this alloy compared to more conventional  $\alpha\beta$ - and  $\beta$ -Ti alloys. They were associated to the absence of damage under the fracture surface.
- Fracture of the TCS alloy was completely ductile and fracture surface morphology indicated a multi-scale fracture mechanism.
- Characteristic length scales of deformation mechanisms have been correlated with characteristic sizes of fracture mechanisms. Twinning remains a major deformation mechanism up to fracture. On the one hand, it explains the large amount of absorbed energy of this alloy. On the other hand, it is probably also responsible for fracture because of the high internal stresses induced by twinning-related deformation incompatibility at a very local scale.

## **6. Acknowledgements**

The authors would like to acknowledge the material support from TIMET and the financial support from Institut Carnot M.I.N.E.S.

## **7. References**

1. C. Brozek, F. Sun, P. Vermaut, et al. *Scr.Mater.* 114 (2016) 60-64.
2. H. Adachi, M. Tsukada, C. Satoko, *J. Phys. Soc. Japan.* 45 (1978) 875-883.
3. ASTM E1820-17 (2017)
4. ISO, BS EN ISO 148-2 (2016) 19 p.
5. E.F. Rauch, M. Véron, J. Portillo, et al. *Microsc. and Anal.* 93 (2008) S5-S8.
6. G. Gilles, Université de Liège, Thesis (2015)
7. T.W. Duerig, G.T. Terlinde, J.C. Williams, *Metall. Trans. A.* 11 (1980) 1987-1998.
8. F. Sun, F. Prima, T. Gloriant, *Mater. Sci. Eng. A.* 527 (2010) 4262-4269.
9. B. Sarre, Université de Technologie de Troyes, Thesis (2017)
10. S. James, Y. Kosaka, R. Thomas, P. Garratt, Eds. Venkatesh et al. *TMS* (2016) 721-725.
11. C. Brozek, Université Pierre et Marie Curie, Thesis (2017)
12. [www.aubertduval.com](http://www.aubertduval.com)
13. H. Tobe, H.Y. Kim, T. Inamura, et al. *Acta Mater.* 64 (2014) 345-355.
14. M.J. Lai, C.C. Tسان, D. Raabe, *Acta Mater.* 111 (2016) 173-186.
15. M. Marteleur, F. Sun, T. Gloriant, et al. *Scr.Mater.* 66 (2012) 749-752.
16. F. Sun, J. Zhang, M. Marteleur, et al. *Acta Mater.* 61 (2013) 6406-6417.
17. M. N. Shiekhelsouk, Université de Lorraine, Thesis (2007)